

Article

Petrogenesis and Metallogenetic Implications of Neoproterozoic Granodiorite in the Super-Large Shimensi Tungsten-Copper Deposit in Northern Jiangxi, South China

Wenfeng Wei ^{1,2} , **Chunkit Lai** ^{3,4,*} , **Bing Yan** ¹, **Xiaoxi Zhu** ¹, **Shengqiong Song** ⁵ and **Lei Liu** ²¹ Institute of Earth Sciences, Chengdu University of Technology, Chengdu 610059, China; weiwenfenghao@163.com (W.W.); yanbing06@cdut.cn (B.Y.); zhuxx97@126.com (X.Z.)² State Key Laboratory of Ore Deposit Geochemistry, Institute of Geochemistry, Chinese Academy of Sciences, Guiyang 550081, China; liulei161@mails.ucas.ac.cn³ Centre of Excellence in Ore Deposits (CODES), University of Tasmania, Tasmania 7001, Australia⁴ Faculty of Science, Universiti Brunei Darussalam, Gadong BE1410, Brunei⁵ Guizhou Land Survey & Plan Institute, Guiyang 550005, China; songye130305180211@163.com

* Correspondence: chunkitl@utas.edu.au; Tel.: +673-879-1488

Received: 13 August 2018; Accepted: 26 September 2018; Published: 29 September 2018



Abstract: The newly discovered Shimensi deposit is a super-large tungsten-copper (W–Cu) deposit with a metal reserve of 742.55 thousand tonnes (kt) W and 403.6 kt Cu. The orebodies are hosted in Mesozoic granites, which intruded the poorly documented Shimensi granodiorite belonging to the Jiuling batholith, the largest intrusion (outcrop > 2500 km²) in South China. Our new SHRIMP (Sensitive High Resolution Ion MicroProbe) zircon dating revealed that the granodiorite at Shimensi (ca. 830–827 Ma) was formed coeval (within analytical uncertainty) or slightly earlier than those in many other places (ca. 819–807 Ma) of the Jiuling batholith. The Neoproterozoic Shimensi granodiorite is peraluminous and high-K calc-alkaline, and contains low P content with no S-type trend (positive P₂O₅ vs. SiO₂ correlation) displayed, thus best classified as peraluminous I-type. The I-type classification is also supported by the zircon REE patterns, largely (93%) positive ε_{Hf(t)} (−0.87 to 6.60) and relatively low δ¹⁸O (5.8–7.7‰). The Neoproterozoic Shimensi granodiorite was formed after the continental arc magmatism (ca. 845–835 Ma), but before the post-collisional S-type granite emplacement (ca. 825–815 Ma) in the Jiangnan Orogen. Therefore, we propose that the Shimensi granodiorite was formed in a collisional/early post-collisional setting. The δ¹⁸O increase from the Shimensi granodiorite to many younger (ca. 819–807 Ma) granodiorites (6.0–8.5‰) in the Jiuling batholith probably reflects an increase of supracrustal rock-derived melts with the progress of collision. The Shimensi granodiorite contains low zircon Ce⁴⁺/Ce³⁺ and Eu/Eu*, suggesting a relatively reducing magma that does not favor porphyry Cu–Au mineralization. This left a high background Cu concentration (avg. 196 ppm) in the Neoproterozoic granodiorite, which may have contributed to the Mesozoic W–Cu mineralization, when the granodiorite is intruded and assimilated by the Mesozoic granites.

Keywords: Shimensi W–Cu deposit; Neoproterozoic granitoids; zircon age and Hf–O isotopes; granite petrogenesis; Jiangnan orogen (South China)

1. Introduction

Northern Jiangxi in South China is a world-class tungsten province [1–7], with its total metal resource estimated to be 4.0 million tonnes (Mt). The two super-large tungsten discoveries (Shimensi

and Zhuxi) in recent years have highlighted significant potential of future prospecting in this region. Current exploration at the Shimensi W–Cu deposit has delineated a metal reserve of 742.55 thousand tonnes (kt) W at 0.195% and 403.6 kt Cu at 0.378% [8], a figure that is likely to grow with further exploration. Previous research was mainly dedicated to the ore-forming Mesozoic granites [9–11], whereas the Proterozoic granodiorite they intruded are rarely studied. Recently, Wei et al. [6] suggested that the copper-rich nature of Shimensi may have been associated with the Proterozoic granodiorite there, into which the Mesozoic granites intruded. In this paper, therefore, we present new data on the petrography, whole-rock geochemistry, together with zircon U–Pb age, trace element and Hf–O isotopes of the Proterozoic granodiorite at Shimensi. With these new data we discuss the petrogenesis and tectonic setting of the Shimensi granodiorite, as well as any metallogenic implications on the Mesozoic W–Cu mineralization.

2. Geological Background

The South China Block (SCB) is composed of the Yangtze block in the northwest, the Cathaysia block in the southeast, and the Jiangnan orogen in between (Figure 1a). The Jiangnan orogen was likely first formed during the Neoproterozoic when extensive arc magmatism occurred [12–18]. Basement rocks of the orogen are dominated by Neoproterozoic, greenschist-facies metamorphosed turbidites and minor arc volcanic rocks of the Shuangqiaoshan Group [19]. Extensive magmatism during the Neoproterozoic and Mesozoic in the Jiangnan orogen have generated numerous granitoids in the orogen [1,18].

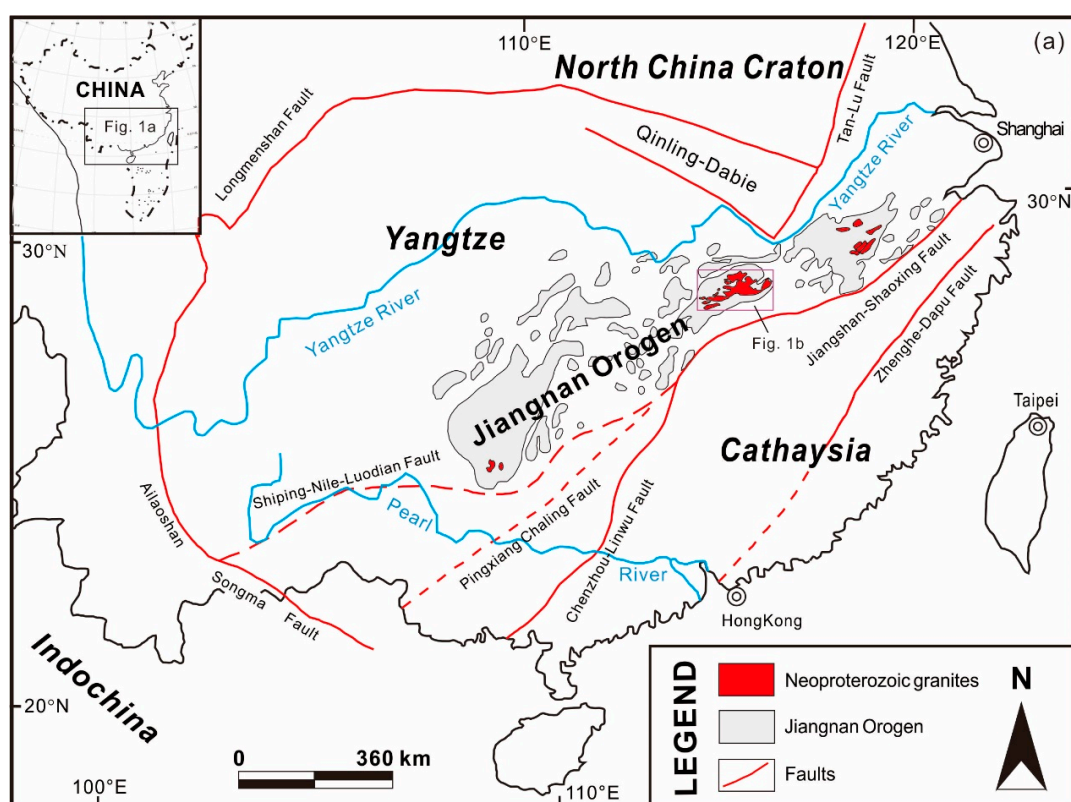


Figure 1. Cont.

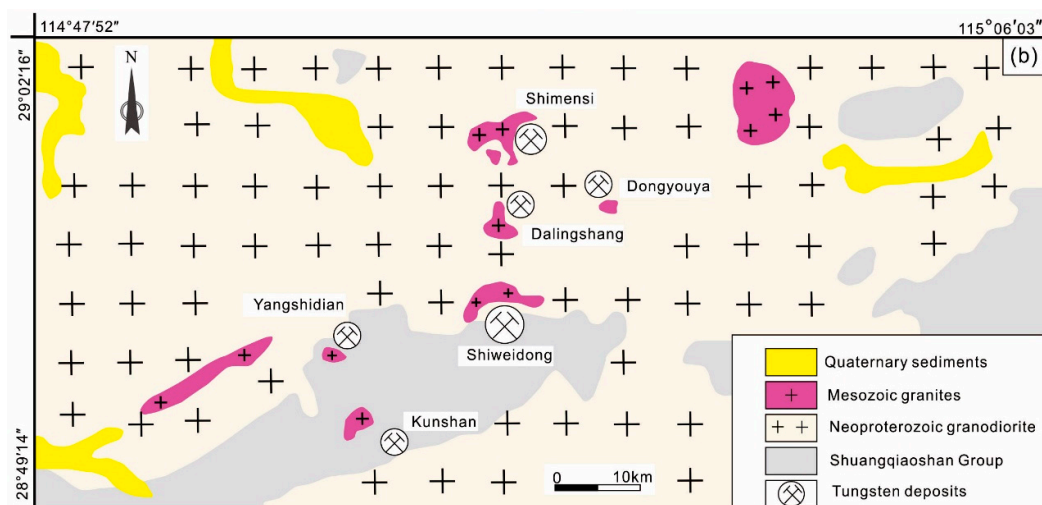


Figure 1. Geologic maps of the (a) Jiangnan Orogen (modified after Song et al. [4]); and (b) Shimensi W-Cu orefield (modified after Gong et al. [20]).

The Neoproterozoic Jiuling granodiorite batholith in the central Jiangnan orogen is the largest intrusion in South China (outcrop > 2500 km²), and is composed mainly of biotite-rich, cordierite-bearing granodiorite [21]. The granodiorite intruded into the Shuangqiaoshan Group contains high W (27 ppm [22], cf. 1 ppm (avg. continental crust) [23]) and Cu (196 ppm [22], cf. 25 ppm (avg. continental crust) [23]) contents, and previous attempts to date the granodiorite yielded very different ages of ca. 807 ± 7 Ma [24] and 819 ± 9 Ma [25]. The Late Mesozoic porphyritic/fine-grained biotite granite and granite porphyry have emplaced into the Neoproterozoic granodiorite and Shuangqiaoshan Group metamorphic rocks [3,4,6,21], and were zircon U-Pb dated to be Late Jurassic to Early Cretaceous (ca. 153–130 Ma) [1,4,6,11]. At Shimensi, both the Neoproterozoic Jiuling granodiorite (locally called the Shimensi granodiorite) and the Late Jurassic–Early Cretaceous granites are exposed (Figure 1b), with the latter generally accepted to be W–Cu ore-forming (Figure 2).

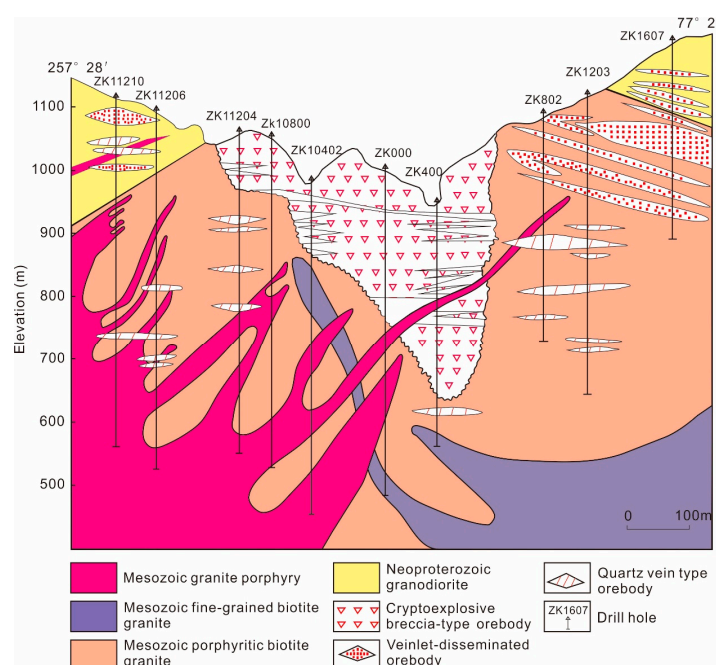


Figure 2. NE-trending cross-section of the Shimensi deposit, showing the three tungsten ore types: Veinlets-disseminated, breccias and veins (modified after Sun and Chen [26]).

3. Sampling and Analytical Methods

Ten representative fresh samples of the Shimensi granodiorite were collected from the adits and drill cores at the Shimensi W–Cu deposit. All the ten samples were analyzed for their whole-rock geochemical compositions, among which three were also analyzed for their zircon U–Pb age, trace element geochemistry and Hf–O isotopes.

This granodiorite is dark gray, medium to coarse-grained and massive. The rocks consist mainly of plagioclase (45–55%), quartz (25–35%) and biotite (15–20%) but no hornblende, as well as minor apatite, zircon and magnetite (Figure 3a–d). These samples are commonly greisen- and sericite-altered.

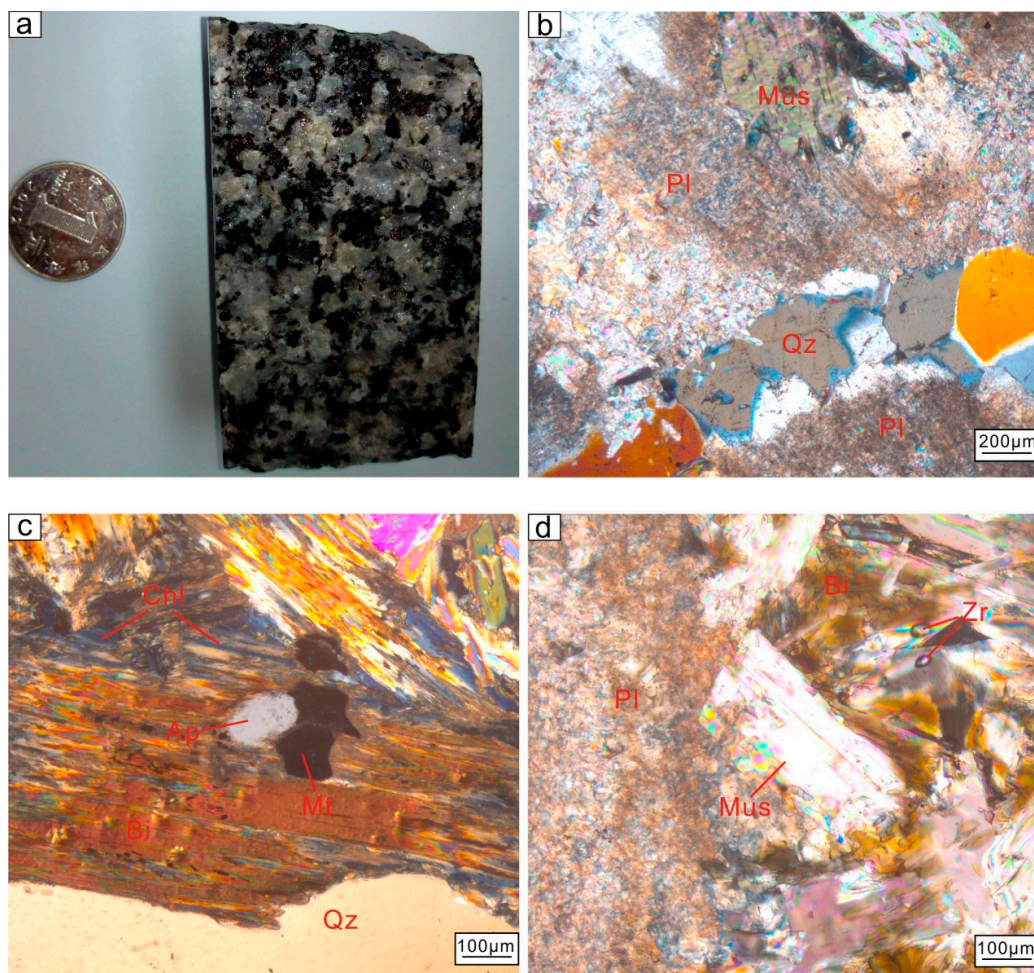


Figure 3. Hand specimen photo and photomicrographs of the Shimensi granodiorite. (a) Hand specimen photo of sample SMS-14; (b) Photomicrograph of sample SMS-12, showing a quartz vein crosscutting the moderately sericite-altered granodiorite; (c) Photomicrograph of sample SMS-15, showing that biotite is partly muscovite- and chlorite-altered with accessory apatite; (d) Photomicrograph of sample SMS-23, which comprises plagioclase, quartz, biotite and muscovite with accessory zircon. Bi = biotite; Mus = muscovite; Pl = plagioclase; Qz = quartz; Chl = chlorite; Ap = apatite; Mt = magnetite; Zr = zircon.

3.1. Whole-Rock Geochemical Analyses

The least altered/weathered representative samples were milled to 200-mesh and then sent to the ALS Laboratory (Guangzhou, China) for major and trace element analyses. Whole-rock major element compositions were determined using X-ray fluorescence (XRF) spectrometry. The samples were mixed with lithium tetraborate and fused ($1100\text{ }^{\circ}\text{C}$ for 15 min) inside a platinum crucible into

glass discs, which were then analyzed by XRF spectrometry. The analytical precisions were better than $\pm 0.01\%$, as estimated from repeated analyses of the standards GSR-1 and GSR-3. Trace element concentrations were measured by inductively coupled plasma-mass spectrometry (ICP-MS), using the method introduced by Liang and Grégoire [27]. Approximately 50 mg of powdered sample was dissolved in 1 mL of distilled HF and 1 mL of HNO₃ in a Teflon-lined stainless-steel bomb. The sealed bombs were then placed in an oven and heated to 190 °C for 24 h. After cooling, the bombs were heated on a hot plate and evaporated to dryness. The residue was then re-dissolved by adding HNO₃, and the bombs were re-sealed and heated at 140 °C for 5 h. The final solutions were transferred into plastic bottles and diluted before the analysis. Two standards (GSR-1, GSR-3) were used to monitor the analytical quality, and the analytical precisions were $\leq 5\%$ for trace elements.

3.2. SHRIMP Zircon U–Pb Dating

Zircon U–Pb geochronology was performed with SHRIMP-II at the Beijing SHRIMP Center of the Chinese Academy of Geological Sciences. Zircons from the rock samples were mounted (epoxy) with the TEMORA (zircon standard sample collection point, a town in the north-east of the Riverina area of New South Wales) zircon standard, and then polished down to half of their thickness to expose their core. The zircon texture and internal structure were studied under the microscope (transmitted-/reflected-light) and cathodoluminescence (CL) imaging. Analysis conditions include 4.5 nA current, 10 kV O^{2–} beam at a 25 μm spot size. Ratios of the U–Th–Pb isotopes were calibrated relative to the TEMORA zircon (²⁰⁶Pb/²³⁸U = 0.0668, corresponding to an age of 417 Ma; [28]). The absolute U–Th–Pb contents were determined relative to the SL13 zircon standard (U = 238 ppm, corresponding to 572 Ma; [29]). Procedures of analysis and data processing follow those outlined in Williams [30]. The ²⁰⁴Pb-method was used to correct the common Pb in the measured Pb isotope compositions. Corrections were negligible and insensitive to how the common Pb composition was chosen, and an average crustal composition [31] that approximates the mineral age was assumed. Data processing was performed with the SQUID 1.03 (an isotope geochronology software) and the Isoplot/Ex2.49 program of Ludwig [32]. Individual analysis uncertainties and the mean ages were reported at 1σ level and 95% confidence level, respectively.

3.3. SHRIMP Analysis of Zircon Oxygen Isotopes

The O-isotope analysis was performed on the U–Pb dated spots using SHRIMP II and a multi-collector (with Cs⁺ primary beam) at the Beijing SHRIMP Center. Conditions and procedures of the analysis follow those outlined in Ickert et al. [33]. Individual analysis uncertainties were reported at 1σ level, and corrections for instrumental mass fractionation and detector gains were performed by referencing to the TEMORA zircon standard.

3.4. LA-MC-ICP-MS Analysis of Zircon Hf Isotopes

The Hf-isotope analysis was performed on the SHRIMP analyzed zircon spots at the Wuhan Sample Solution Analytical Technology Co. Ltd. (Wuhan, China), using a GeolasPro 193 nm ArF Excimer laser ablation system coupled to a multi-collector (MC)-ICP-MS. Analytical conditions include 44 μm laser beam size, 10 Hz repetition rate and 8 J/cm² energy density.

Ratios of Yb and Hf isotopes were normalized, respectively, to ¹⁷²Yb/¹⁷³Yb = 1.35274 and ¹⁷⁹Hf/¹⁷⁷Hf = 0.7325 [34], using an exponential law for mass fractionation. Routine run of the 91,500 zircon standard yielded a weighted mean ¹⁷⁶Hf/¹⁷⁷Hf = 0.282306 ± 31 (2σ), consistent with the recommended value (0.282306 ± 10 (2σ); [35]). The εHf(t) values were calculated by using the decay constant of 1.867 × 10⁻¹¹ [35] and the chondritic uniform reservoir values (CHUR, ¹⁷⁶Lu/¹⁷⁷Hf = 0.0336, ¹⁷⁶Hf/¹⁷⁷Hf = 0.282785; [36]). Initial ¹⁷⁶Hf/¹⁷⁷Hf and εHf(t) values were calculated with the corresponding ²⁰⁶Pb/²³⁸U ages. The mantle extraction model (TDM) age was calculated by using the initial zircon ¹⁷⁶Hf/¹⁷⁷Hf at the time of crystallization (apparent ²⁰⁶Pb/²³⁸U age) by using ¹⁷⁶Hf/¹⁷⁷Hf

$= 0.28325$ and $^{176}\text{Lu}/^{177}\text{Hf} = 0.0384$ for the bulk earth [36], and $^{176}\text{Lu}/^{177}\text{Hf} = 0.015$ for the average crust [37].

3.5. LA-ICP-MS Analysis of Zircon Trace Element Geochemistry

The zircon trace element compositions were measured at the Wuhan Sample Solution Analytical Technology Co. Ltd., using a GeolasPro 193 nm ArF Excimer laser ablation system coupled with an Agilent 7700 \times Quadrupole ICP-MS (equipped with an ion-counting system). All the analyses were carried out with a 44 μm beam diameter, 5 Hz repetition rate, and 8 J/cm 2 beam energy. Procedures and conditions of the analysis follow those outlined in Liu et al. [38]. NIST SRM-610 was used as an external standard during the analysis session. The offline selection, time-drift correction, background and analytical signal integration, and quantitative trace element calibration were conducted using GLITTER [39].

4. Results

4.1. Whole-Rock Geochemistry

Geochemical compositions of the Shimensi granodiorite samples are shown in Table 1. The rocks contain 66.4–69.4 wt % SiO₂, 13.7–16.2 wt % Al₂O₃, 1.40–1.92 wt % MgO, 4.14–5.40 wt % Fe₂O₃^T, and 3.0–5.2 wt % K₂O. Loss on ignition (LOI) is below 3 wt % and shows no correlation with mobile element (e.g., K) contents, thus it is assumed that alteration influence on the latter is minimal. The rocks are high-K calc-alkaline and peraluminous, with A/CNK (molar Al₂O₃/(CaO + Na₂O + K₂O)) of 1.3–1.9. On the Harker diagrams (Figure 4), the TiO₂, Fe₂O₃^T, MgO, CaO, and Al₂O₃ contents are negatively correlated with SiO₂.

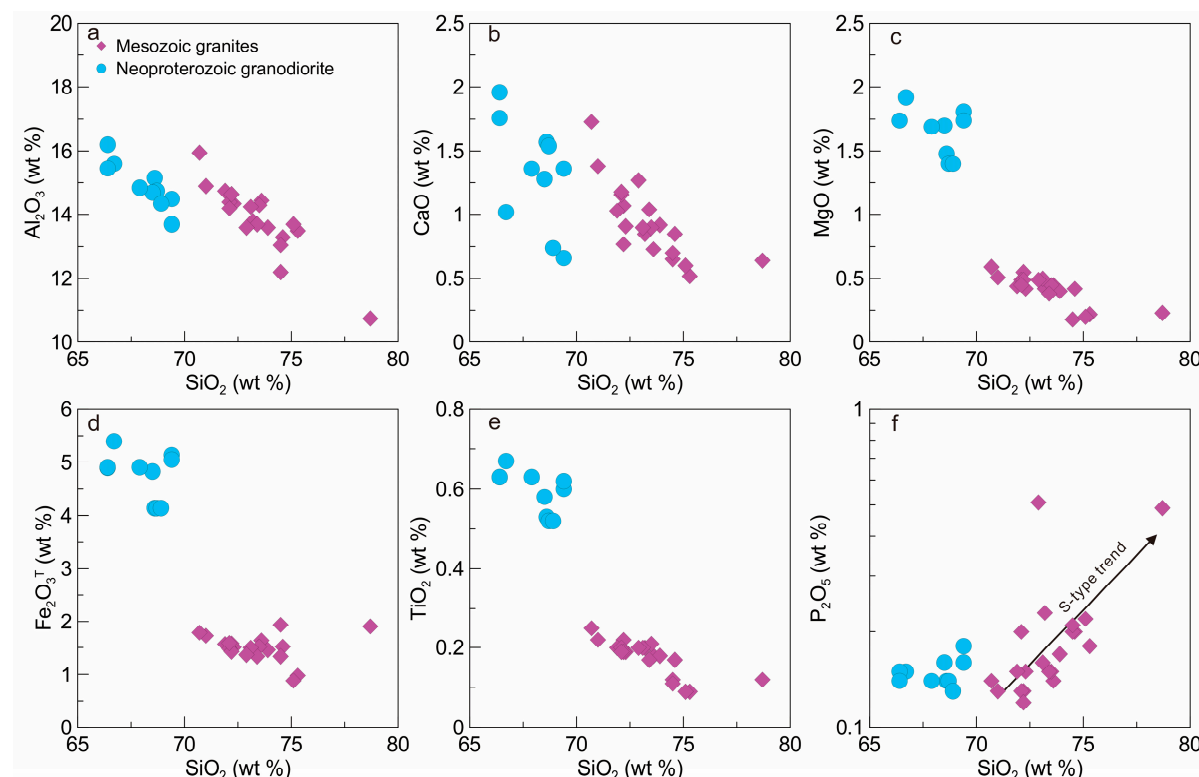


Figure 4. Cont.

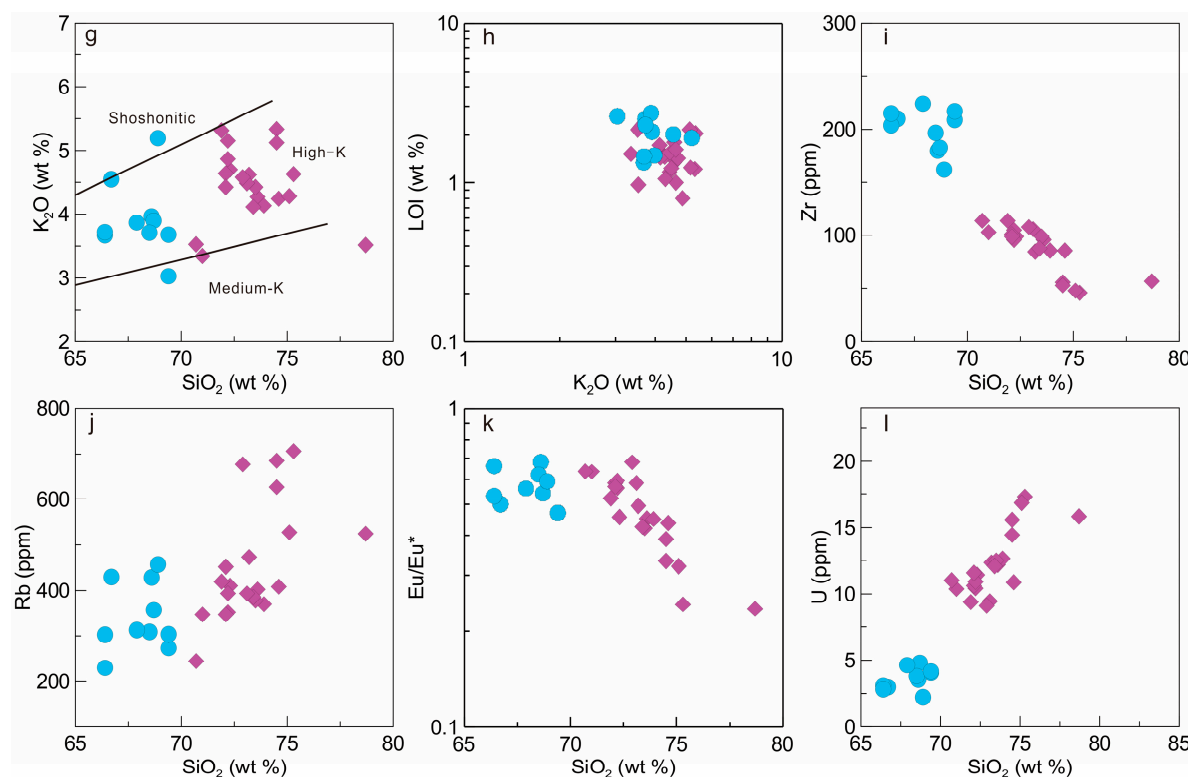


Figure 4. Harker diagrams for the Shimensi granodiorite. Data of the ore-related Mesozoic Shimensi granites are from Wei et al. [6].

Table 1. Major element contents of the Shimensi granodiorite (wt %).

Sample	SiO ₂	TiO ₂	Al ₂ O ₃	Fe ₂ O ₃ ^T	MnO	MgO	CaO	Na ₂ O	K ₂ O	P ₂ O ₅	LOI	Total	A/CNK
SMS-1	66.7	0.67	15.60	5.40	0.09	1.92	1.02	1.61	4.55	0.15	2.01	100.05	1.7
SMS-2	69.4	0.60	14.50	5.14	0.08	1.81	0.66	1.82	3.03	0.18	2.60	100.00	1.9
SMS-20	66.4	0.63	16.20	4.90	0.09	1.74	1.96	2.58	3.67	0.15	1.33	99.80	1.4
SMS-22	68.6	0.53	15.15	4.14	0.08	1.48	1.57	2.60	3.97	0.14	1.48	99.93	1.3
SMS-12	68.7	0.52	14.75	4.14	0.08	1.40	1.54	2.34	3.90	0.14	2.09	99.92	1.4
SMS-14	68.5	0.58	14.70	4.83	0.08	1.70	1.28	1.88	3.71	0.16	2.50	100.05	1.6
SMS-15	67.9	0.63	14.85	4.91	0.09	1.69	1.36	1.80	3.87	0.14	2.72	100.10	1.5
SMS-23	66.4	0.63	15.45	4.91	0.09	1.74	1.76	2.05	3.72	0.14	2.30	99.58	1.5
SMS-25	69.4	0.62	13.70	5.05	0.09	1.74	1.36	1.96	3.68	0.16	1.46	99.37	1.4
SMS-26	68.9	0.52	14.35	4.14	0.08	1.40	0.74	1.76	5.20	0.13	1.91	99.29	1.5

The samples exhibit similar total rare earth element (REE) contents (129–171 ppm) and consistent REE patterns. In the chondrite-normalized REE diagram (Table 2, Figure 5), the granodiorite samples are light REE (LREE) enriched, with mild LREE/HREE fractionation ($(\text{La}/\text{Yb})_{\text{N}} = 6.3\text{--}9.2$) and slightly negative Eu anomalies ($\text{Eu}/\text{Eu}^* = 0.47\text{--}0.68$; $\text{Eu}/\text{Eu}^* = \text{Eu}_{\text{N}}/(\text{Sm}_{\text{N}} \times \text{Gd}_{\text{N}})^{1/2}$; [40]). In the primitive mantle-normalized multi-element diagram (Figure 6), the samples are enriched in large ion lithophile elements (LILEs, e.g., Rb and K) and depleted in high-strength field elements (HFSEs, e.g., Nb, Ta, Zr and Hf) with negative Ba, Nb–Ta and Ti anomalies.

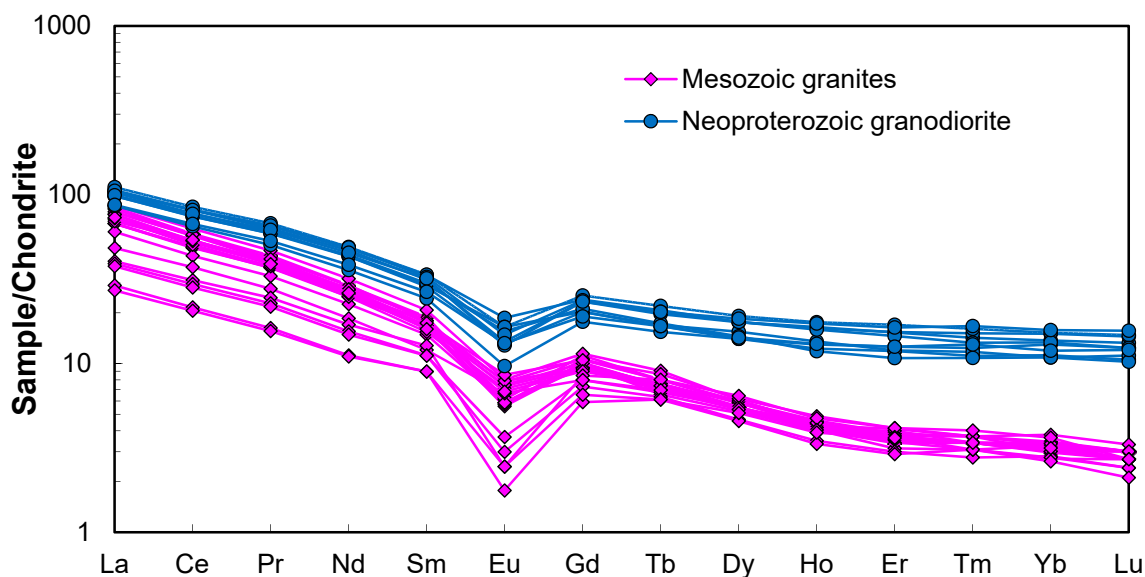


Figure 5. Chondrite-normalized REE patterns of the Shimensi granodiorite. Normalization values are from Sun and McDonough [41]. Data of the ore-related Mesozoic Shimensi granites are from Wei et al. [6].

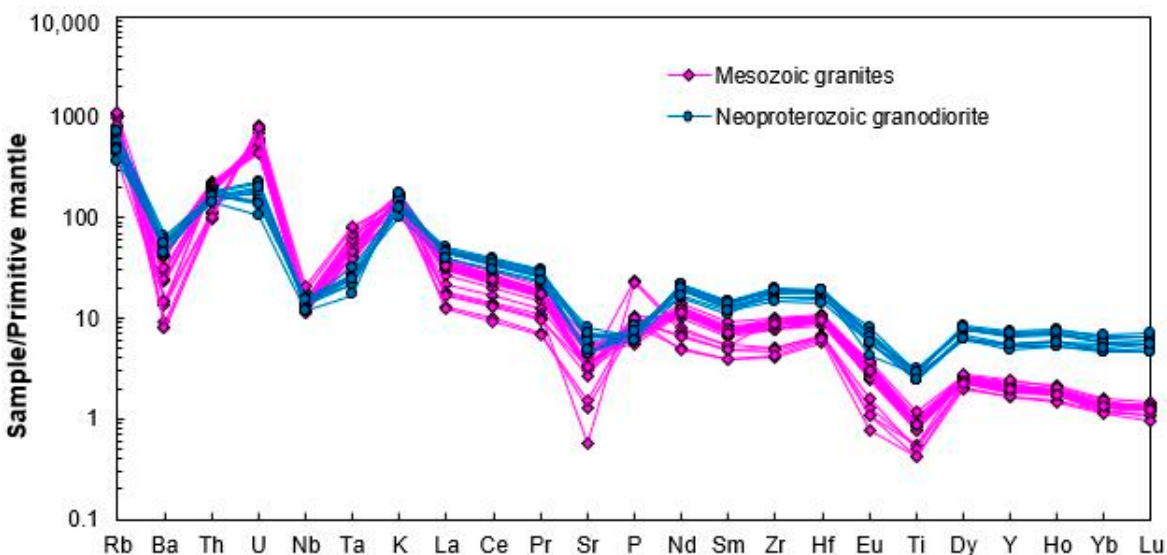


Figure 6. Primitive mantle-normalized multi-element diagrams of the Shimensi granodiorite. Normalization values are from Sun and McDonough [41]. Data of the ore-related Mesozoic Shimensi granites are from Wei et al. [6].

Table 2. Trace element contents of the Shimensi granodiorite (ppm).

Sample	SMS-1	SMS-2	SMS-20	SMS-22	SMS-12	SMS-14	SMS-15	SMS-23	SMS-25	SMS-26
Rb	430	274	230	429	357	309	313	303	304	457
Sr	95.5	92.9	143.0	173.0	139.5	139.0	126.0	147.0	92.2	103.5
Zr	210	209	204	180	183	197	224	215	217	162
Nb	11.5	10.7	10.6	9.7	11.0	9.8	10.6	10.9	10.9	8.6
Ba	458.0	315.0	428.0	392.0	323.0	394.0	389.0	389.0	318.0	382.0
La	32.2	26.7	33.0	31.9	30.5	30.6	34.4	32.7	30.8	27.0
Ce	65.5	52.5	65.9	62.7	60.4	60.1	68.6	65.6	62.3	54.2
Pr	7.71	6.15	7.95	7.38	7.18	7.22	8.26	8.02	7.55	6.50
Nd	28.1	21.5	28.9	25.9	25.9	26.4	29.4	29.2	27.2	23.1
Sm	6.12	4.74	6.53	5.67	5.58	5.82	6.55	6.35	6.23	5.19
Eu	0.99	0.71	1.37	1.21	0.96	1.14	1.21	1.09	0.94	0.97
Gd	6.03	4.58	6.19	5.26	5.23	5.47	6.55	6.14	6.03	4.92
Tb	0.93	0.73	0.98	0.79	0.80	0.82	1.04	0.96	0.96	0.79
Dy	5.66	4.51	5.68	4.52	4.97	4.67	6.16	5.68	5.93	4.59
Ho	1.18	0.93	1.16	0.88	0.97	0.85	1.26	1.14	1.24	0.94
Er	3.21	2.64	3.23	2.49	2.51	2.26	3.56	3.06	3.43	2.64
Tm	0.46	0.40	0.49	0.36	0.38	0.35	0.52	0.43	0.54	0.42
Yb	2.86	2.71	3.14	2.34	2.27	2.27	3.18	2.79	3.30	2.49
Lu	0.44	0.41	0.48	0.35	0.37	0.34	0.49	0.41	0.52	0.40
Y	30.60	25.10	30.90	23.90	25.20	22.40	34.20	29.50	32.40	25.20
Hf	5.6	5.7	5.4	4.8	5.0	5.6	5.8	5.9	5.9	4.3
Ta	1.1	1.1	1.0	1.0	1.3	0.9	0.9	1.0	1.0	0.7
W	43	100	12	18	31	7	9	797	21	31
Th	14.2	13.3	13.5	14.7	15.5	12.1	14.7	14.5	13.9	12.0
U	3.0	4.1	3.1	3.5	4.8	3.8	4.7	2.8	4.2	2.2
Σ REE	161.39	129.21	165.00	151.75	148.02	148.31	171.18	163.57	156.97	134.15
La _N /Yb _N	7.6	6.6	7.1	9.2	9.1	9.1	7.3	7.9	6.3	7.3
Eu/Eu*	0.50	0.47	0.66	0.68	0.54	0.62	0.56	0.53	0.47	0.59

4.2. Zircon U–Pb Ages

Zircons from the Shimensi granodiorite are colorless and transparent, 50 to 200 μm long with aspect ratios of 1:1–3:1. Under CL imaging, all measured zircons have well-developed oscillatory zoning with no residual cores or metamorphic rims (Figure 7). The zircons have varying Th contents (16–339 ppm) and low to medium U contents (124–665 ppm), with most Th/U ratios clustering between 0.13–0.73 (Table 3). All these textural and geochemical features suggest a magmatic origin for the zircons [42].

Nine spot analyses on 9 zircons from sample SMS-2 yielded $^{206}\text{Pb}/^{238}\text{U}$ ages of 811 ± 13 Ma to 852 ± 14 Ma and a weighted mean age of 830 ± 13 Ma (MSWD = 1.6, Figure 8). The seven analyzed zircons (808 ± 12 Ma to 840 ± 12 Ma) from sample SMS-12 yielded a weighted mean $^{206}\text{Pb}/^{238}\text{U}$ age of 827 ± 10 Ma (MSWD = 1.1; Figure 8). The four zircons analyzed (809 ± 15 Ma to 841 ± 15 Ma) from sample SMS-23 yielded a weighted mean $^{206}\text{Pb}/^{238}\text{U}$ age of 828 ± 14 Ma (MSWD = 1.03) (Figure 8).

Therefore, we suggest that the granodiorite was emplaced during ca. 827 to 830 Ma.

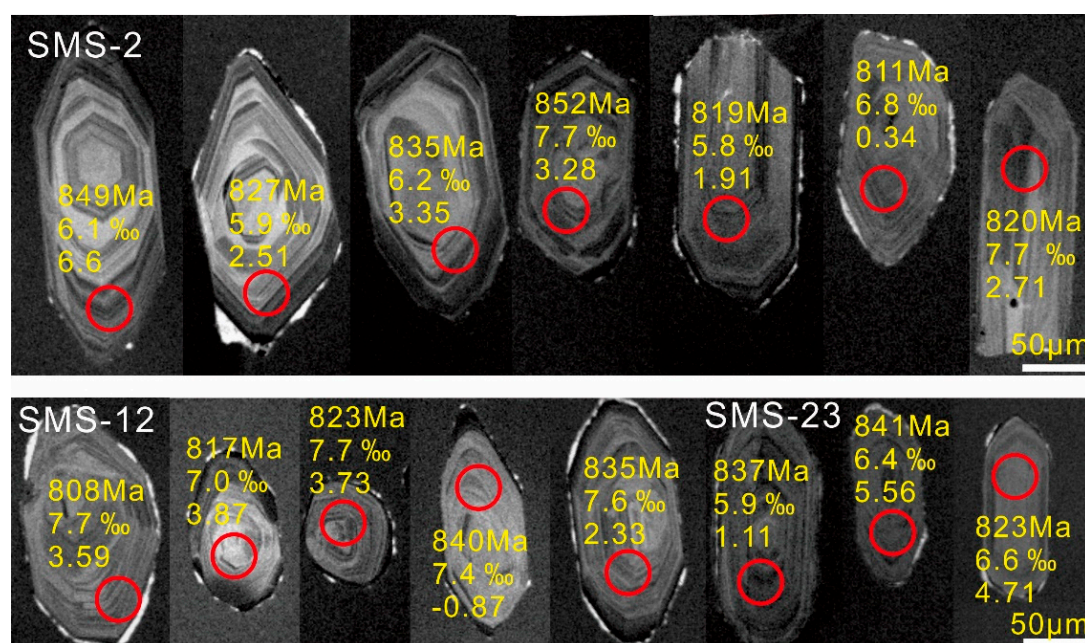


Figure 7. CL images of representative zircons from the Neoproterozoic Shimensi granodiorite. Yellow numbers (from top to bottom) denote the U–Pb age, $\delta^{18}\text{O}$ and $\epsilon\text{Hf(t)}$, respectively. Red circles show the analysis spots.

Table 3. SHRIMP zircon U–Pb data of the Shimensi granodiorite.

Spot	$^{206}\text{Pb}_\text{c}$ (%)	U (ppm)	Th (ppm)	$^{232}\text{Th}/^{238}\text{U}$	$^{206}\text{Pb}^*$ (ppm)	$^{207}\text{Pb}^*/^{206}\text{Pb}^*$	1 σ (%)	$^{207}\text{Pb}^*/^{235}\text{U}$	1 σ (%)	$^{206}\text{Pb}^*/^{238}\text{U}$	1 σ (%)	$^{206}\text{Pb}/^{238}\text{U}$ Age (Ma)
SMS-2, mean = 830 ± 13 Ma, MSWD = 1.6, n = 9												
1	0.08	341	95	0.29	41.3	0.0659	1.3	1.279	2.2	0.1408	1.7	849 ± 14
2	0.11	245	25	0.11	28.8	0.0646	1.9	1.220	2.6	0.1369	1.8	827 ± 14
3	0.39	157	66	0.43	18.7	0.0636	3.0	1.213	3.6	0.1384	2.0	835 ± 16
4	0.12	293	44	0.15	35.7	0.0692	1.9	1.349	2.6	0.1414	1.8	852 ± 14
5	0.00	650	339	0.54	78.9	0.0668	1.0	1.301	1.9	0.1412	1.7	851 ± 13
6	0.01	286	41	0.15	33.3	0.0665	1.9	1.241	2.6	0.1354	1.7	819 ± 13
7	0.00	332	46	0.14	38.2	0.0668	1.4	1.234	2.3	0.1340	1.9	811 ± 14
8	—	404	229	0.59	47.0	0.0666	1.3	1.245	2.2	0.1356	1.7	820 ± 13
9	0.16	292	37	0.13	33.7	0.0643	1.8	1.188	2.5	0.1340	1.7	811 ± 13
SMS-12, mean = 827 ± 10 Ma, MSWD = 1.1, n = 7												
1	0.02	337	45	0.14	38.7	0.0660	1.4	1.216	2.1	0.1336	1.6	808 ± 12
2	0.21	221	75	0.35	26.0	0.0658	2.1	1.239	2.7	0.1365	1.7	825 ± 13
3	0.00	665	68	0.11	77.2	0.0660	0.9	1.230	1.8	0.1352	1.6	817 ± 12
4	0.02	193	136	0.73	22.9	0.0679	2.1	1.296	2.7	0.1385	1.7	836 ± 13
5	—	306	39	0.13	35.7	0.0667	1.5	1.252	2.2	0.1361	1.6	823 ± 12
6	0.23	567	87	0.16	68.0	0.0655	1.3	1.258	2	0.1393	1.5	840 ± 12
7	—	225	29	0.13	26.7	0.0682	2.9	1.301	3.3	0.1383	1.6	835 ± 13
SMS-23, mean = 828 ± 14 Ma, MSWD = 1.03, n = 4												
1	0.01	292	39	0.14	34.7	0.0688	1.5	1.316	2.3	0.1387	1.7	837 ± 14
2	—	124	53	0.44	14.8	0.0666	2.3	1.281	3	0.1394	1.9	841 ± 15
3	0.3	163	88	0.56	18.8	0.0584	4.2	1.077	4.6	0.1337	1.9	809 ± 15
4	—	328	16	0.05	38.4	0.0669	1.3	1.255	2.2	0.1362	1.7	823 ± 13

* radiogenic portions.

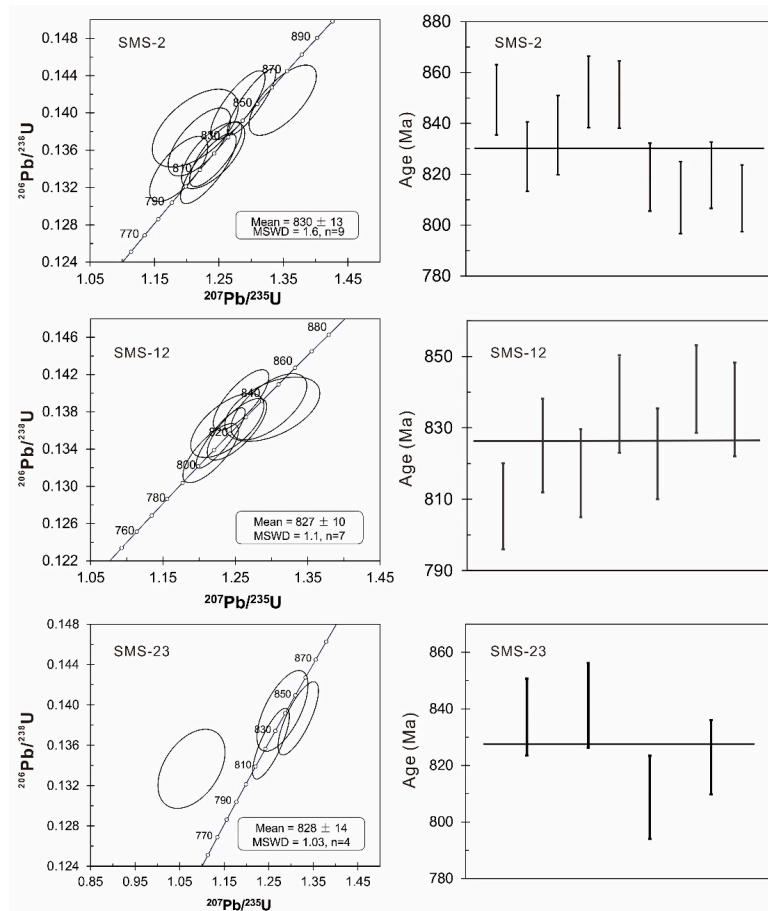


Figure 8. SHRIMP zircon U-Pb concordia diagram of the Shimensi granodiorite.

4.3. Zircon Hf–O Isotopes

A total of 15 Hf–O isotope measurements were conducted on 15 zircon grains (Table 4). Zircon $\delta^{18}\text{O}$ values vary from 5.8‰ to 7.7‰ (mean: 6.8‰) (Figure 9). The zircon $\varepsilon\text{Hf(t)}$ values vary from −0.87 to 6.60 (mean: 2.98), of which 93% are positive (Figure 9).

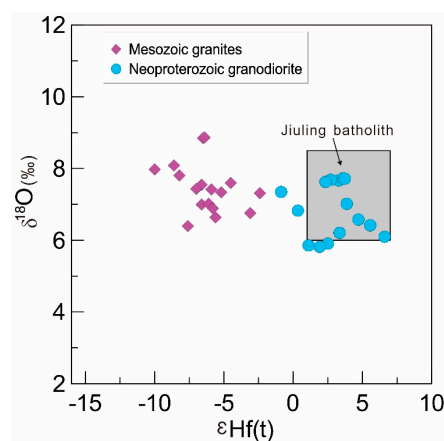


Figure 9. $\varepsilon\text{Hf(t)}$ vs. $\delta^{18}\text{O}$ for the zircons from the Shimensi granodiorite. Data of the ore-related Mesozoic Shimensi granites are from Wei et al. [6]. Jiuling batholith data are from Zhao et al. [24], Li et al. [25], Wang et al. [43].

Table 4. Zircon Hf–O isotope data of the Shimensi granodiorite.

Spot	$^{176}\text{Yb}/^{177}\text{Hf}$	2σ	$^{176}\text{Lu}/^{177}\text{Hf}$	2σ	$^{176}\text{Hf}/^{177}\text{Hf}$	2σ	t (Ma)	$\varepsilon_{\text{Hf}}(t)$	$f_{\text{Lu/Hf}}$	$T_{\text{DM1}} (\text{Ma})$	$T_{\text{DM2}} (\text{Ma})$	$\delta^{18}\text{O} (\text{\textperthousand})$	$\pm \text{\textperthousand}$
SMS-2													
1	0.091007	0.0018005	0.0019188	0.0000235	0.2824591	0.0000194	849	6.60	-0.94	1150	1318	6.1	0.2
2	0.040921	0.0002453	0.0008791	0.0000037	0.2823405	0.0000181	827	2.51	-0.97	1284	1558	5.9	0.2
3	0.082770	0.0004998	0.0018237	0.0000159	0.2823742	0.0000202	835	3.35	-0.95	1269	1512	6.2	0.2
4	0.077641	0.0018125	0.0016481	0.0000423	0.2823591	0.0000196	852	3.28	-0.95	1284	1529	7.7	0.3
6	0.082227	0.0001336	0.0016951	0.0000073	0.2823409	0.0000205	819	1.91	-0.95	1312	1590	5.8	0.2
7	0.058475	0.0005013	0.0011958	0.0000071	0.2822939	0.0000223	811	0.34	-0.96	1361	1682	6.8	0.2
8	0.052659	0.0038467	0.0010774	0.0000726	0.2823535	0.0000203	820	2.71	-0.97	1273	1540	7.7	0.2
SMS-12													
1	0.100158	0.0006790	0.0021757	0.0000104	0.2824024	0.0000184	808	3.59	-0.93	1240	1476	7.7	0.2
3	0.060693	0.0016232	0.0012169	0.0000264	0.2823903	0.0000202	817	3.87	-0.96	1226	1465	7.0	0.2
5	0.072390	0.0005023	0.0015484	0.0000135	0.2823876	0.0000183	823	3.73	-0.95	1240	1479	7.7	0.1
6	0.087255	0.0009749	0.0018199	0.0000227	0.2822507	0.0000203	840	-0.87	-0.95	1445	1782	7.4	0.2
7	0.055225	0.0009956	0.0011990	0.0000351	0.2823362	0.0000193	835	2.33	-0.96	1301	1575	7.6	0.2
SMS-23													
1	0.069315	0.0001253	0.0014777	0.0000064	0.2823042	0.0000175	837	1.11	-0.96	1356	1654	5.9	0.2
2	0.075810	0.0006502	0.0017100	0.0000095	0.2824312	0.0000201	841	5.56	-0.95	1184	1377	6.4	0.3
4	0.067762	0.0013936	0.0015192	0.0000307	0.2824150	0.0000210	823	4.71	-0.95	1200	1417	6.6	0.1

4.4. Zircon Trace Element Compositions

All the zircons analyzed have similar ranges of U and Th concentrations (108 to 1019 ppm and 31 to 1928 ppm, respectively) and Th/U ratios (0.08 to 1.89, mostly <0.6) (Table 5). Tungsten concentration of the zircons ranges from 0 to 14,294 ppm (average 2718 ppm).

Chondrite-normalized zircon REE patterns for all the samples are featured by distinct depletion of LREEs ($(\text{La}/\text{Yb})_{\text{N}} = 0.000002\text{--}0.014807$), positive Ce and negative Eu anomalies ($\text{Eu}/\text{Eu}^* = 0.01\text{--}0.13$; mean = 0.07) (Table 5; Figure 10), typical of igneous origin [44,45]. Due to the relatively low zircon La and Pr concentrations (Table 5), and to the susceptibility of contamination by tiny inclusions of minerals or melt [45], the $\text{Ce}^{4+}/\text{Ce}^{3+}$ values (instead of the conventional La–Pr interpolation) were adopted. $\text{Ce}^{4+}/\text{Ce}^{3+}$ values of the zircons were calculated using the lattice-strain model proposed by Ballard et al. [46] and Trail et al. [47] (Table 5; Figure 10). The Shimensi granodiorite samples have zircon $\text{Ce}^{4+}/\text{Ce}^{3+}$ values of 4.05 to 128.64 (average 38.84).

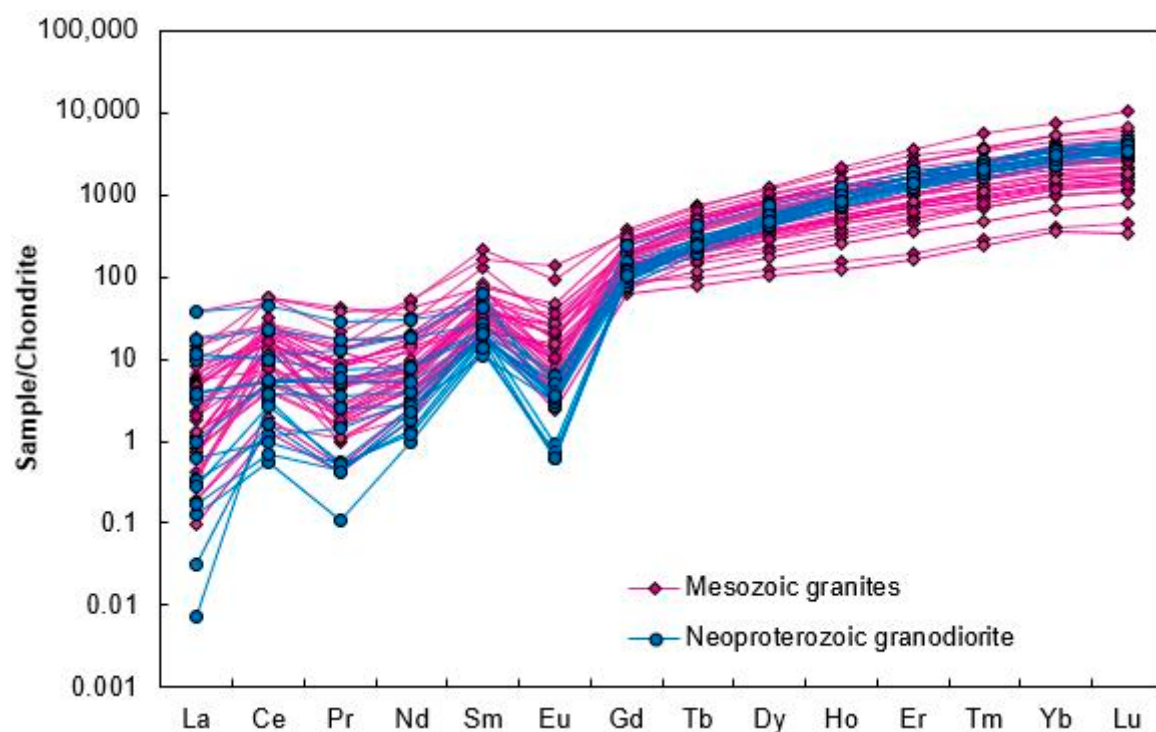


Figure 10. Chondrite-normalized zircon REE patterns of the Shimensi granodiorite. Chondrite normalization values are from Sun and McDonough [41]. Data of the ore-related Mesozoic Shimensi granites are from Wei et al. [6].

Table 5. LA-ICP-MS zircon trace element contents of the Shimensi granodiorite (ppm).

Spot	Th	U	W	La	Ce	Pr	Nd	Sm	Eu	Gd	Tb	Dy	Ho	Er	Tm	Yb	Lu	Eu/Eu*	Ce ⁴⁺ /Ce ³⁺	Ce/Ce*
SMS-2																				
1	63	169	0	0.0023	2.5	0.06	0.84	3.13	0.38	28.63	11.21	148	60.98	294	65.78	631	118	0.12	31.37	51.22
2	39	233	0.2	0.1015	0.95	0.18	1.82	3.87	0.07	27.69	11.74	158	61.66	297	65.97	607	110	0.02	4.49	1.69
3	57	223	212	0.0894	2.17	0.07	1.49	3.45	0.27	29.53	12.58	173	70.28	355	81.63	781	149	0.08	17.96	6.60
4	41	278	3509	0.9973	3.03	0.44	2.45	3.14	0.22	28.46	13.12	187	75.84	369	83.40	809	143	0.07	17.10	1.10
6	39	263	3.78	0.0405	0.45	0.01	0.57	2.35	0.05	23.85	10.96	160	63.08	311	69.26	634	130	0.02	9.42	5.38
7	173	320	8.65	11.9543	36.3	3.49	18.20	8.35	0.41	39.57	13.64	160	59.82	279	59.67	544	115	0.07	15.10	1.35
8	118	219	0.11	2.9547	8.68	1.60	11.30	12.30	0.20	62.53	20.39	243	88.03	407	82.44	733	149	0.02	4.05	0.96
SMS-12																				
1	45	210	556	0.0537	0.56	0.05	1.11	3.42	0.04	29.45	12.21	158	63.72	303	66.41	622	117	0.01	5.81	2.60
3	1928	1019	14294	5.3120	18.70	2.15	10.90	5.18	0.45	20.58	8.97	133	56.12	280	64.85	613	110	0.13	27.29	1.33
5	35	462	498	0.3031	4.18	0.30	1.64	2.08	0.23	23.10	10.71	152	60.92	301	68.90	618	132	0.10	52.31	3.34
6	49	411	10164	3.5358	8.10	0.89	4.91	4.54	0.37	32.60	14.15	184	69.19	335	73.85	697	137	0.09	23.53	1.10
7	31	295	2788	1.2250	4.27	0.66	3.19	3.61	0.29	27.02	11.4	139	51.79	250	53.60	488	102	0.09	16.80	1.14
SMS-23																				
1	36	244	14.4	0.1874	0.77	0.07	0.74	2.64	0.04	25.52	11.94	154	60.77	285	63.06	592	109	0.02	128.64	1.62
2	50	108	0.06	0.0099	1.31	0.05	1.37	3.71	0.24	29.36	10.56	134	54.27	266	59.59	568	111	0.07	101.73	14.17
4	142	911	8723	1.1677	4.62	0.70	4.64	4.02	0.26	27.42	11.51	155	60.41	290	65.35	634	111	0.08	127.04	1.23

5. Discussion

5.1. Age and Geochemistry of the Shimensi Granodiorite

Prior to this study, there are only two published ages for the Jiuling granodiorite batholith (i.e., 807 ± 7 Ma and 819 ± 9 Ma; [24,25]). The three Shimensi granodiorite age data we obtained (830–827 Ma) are coeval (within analytical uncertainty) or slightly older than the previously reported ages of the Jiuling granodiorite.

Geochemistry of the Neoproterozoic Shimensi granodiorite is very different from the Mesozoic Shimensi granites. Although both belong to high-K calc-alkaline series, the Neoproterozoic granodiorite is considerably less fractionated ($\text{SiO}_2 < 70$ wt %), and contains higher $\text{MgO} (>0.75$ wt %), $\text{Fe}_2\text{O}_3^T (>4$ wt %) and $\text{TiO}_2 (>0.5$ wt %) than the Mesozoic intrusions. Many Neoproterozoic Shimensi granodiorite samples are also more peraluminous than the Mesozoic Shimensi granites (Figure 11). In terms of zircon trace element compositions, those of the Neoproterozoic granodiorite contain similar Ce/Ce^* but lower Eu/Eu^* than their Mesozoic granite counterparts (Figure 12). This indicates that the Neoproterozoic granodiorite is less fractionated than the Mesozoic granites, and that both rock types were formed under similar reducing conditions. In the whole-rock chondrite-normalized REE diagram, the Neoproterozoic granodiorite is less fractionated ($(\text{La}/\text{Yb})_N < 9.2$) and contains higher total REE contents (>129 ppm) than the Mesozoic granites (Figure 5). In the primitive mantle-normalized multi-element diagram, the Neoproterozoic granodiorite is more enriched in HFSEs (e.g., Ti, Dy, Y, Ho, Yb and Lu), and with less distinctive negative Sr anomaly than the Mesozoic granites (Figure 6).

Although strongly peraluminous, as indicated by the presence of biotite and cordierite and by the A/NK vs. A/CNK diagram (Figure 11), the Neoproterozoic granodiorite samples do not show an S-type trend in the P_2O_5 vs. SiO_2 diagram (Figure 4f). In fact, I-type granites can also be peraluminous [48]. In the zircon chondrite-normalized REE diagrams (Figures 6 and 13), the Neoproterozoic granodiorite contains lower REE contents than the Mesozoic Shimensi granites and the average granitoid, but similar REE contents (and higher Eu/Eu^*) than the average dolerite [49]. The Neoproterozoic granodiorite datapoints also fall inside/close to the average dolerite field in Figure 12. This suggests that the granodiorite was likely derived from a doleritic source rock, and is thus most likely I-type. The facts that the granodiorite lacks inherited zircons (Figure 7; Table 3), and contains relatively low zircon $\delta^{18}\text{O}$ (5.8–7.7‰; mean: 6.8‰), and mostly (93%) positive zircon $\epsilon\text{Hf(t)}$ values, all demonstrate its peraluminous I-type affinity.

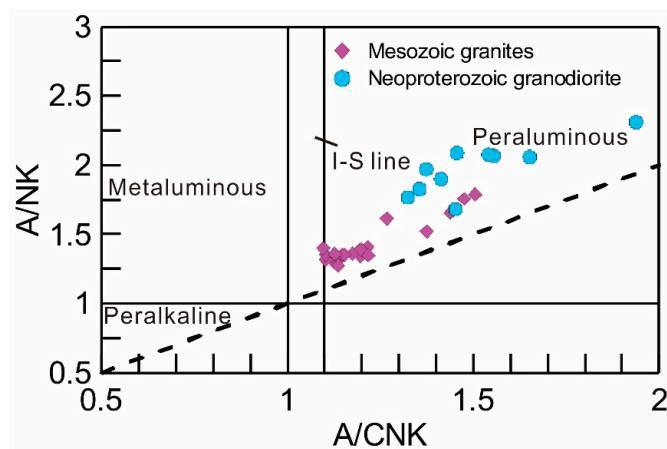


Figure 11. A/CNK vs. A/NK diagram. Data of the ore-related Mesozoic Shimensi granites are from Wei et al. [6].

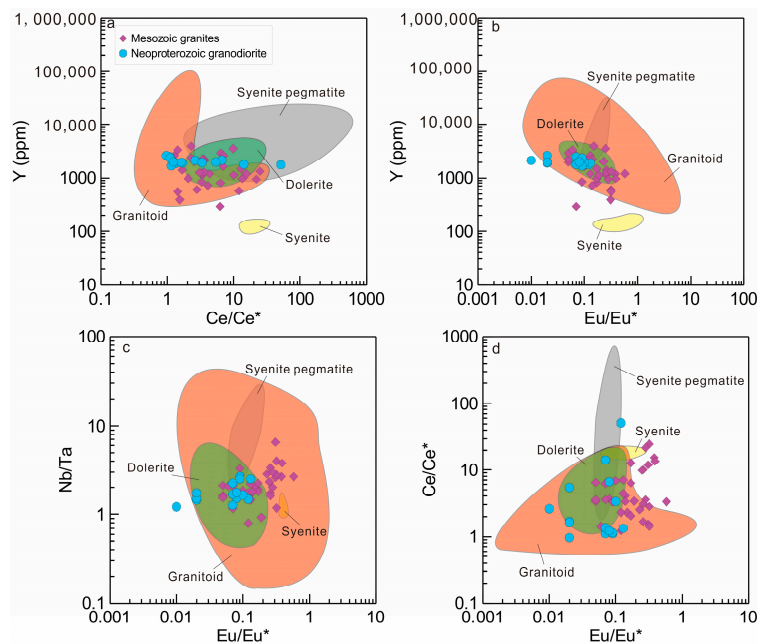


Figure 12. Zircon trace element correlations for the Shimensi granodiorite. Data of the ore-related Mesozoic Shimensi granites are from Wei et al. [6]. Data of the zircons from different igneous rock types are from [49].

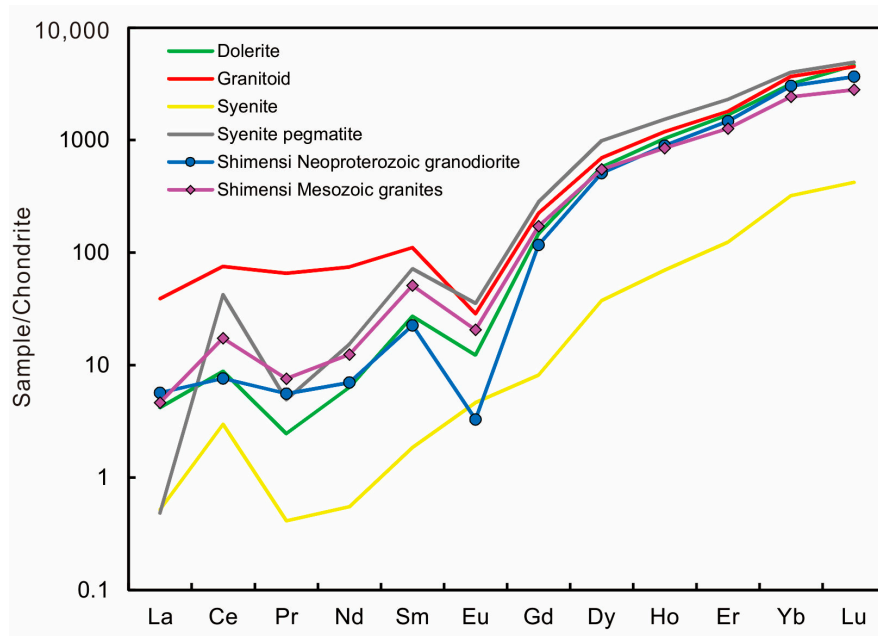


Figure 13. Chondrite-normalized averaged zircon REE patterns for the Shimensi granodiorite. Data of the ore-related Mesozoic Shimensi granites are from Wei et al. [6]. Data of the zircons from different igneous rock types are from [49].

5.2. Petrogenesis and Metallogenic Implications of the Shimensi Granodiorite

In the Jiangnan Orogen, the Shimensi granodiorite (830–827 Ma) was formed after the continental arc-type Jianxichong volcano-sedimentary rocks (845–835 Ma; [50]), and before the post-collisional S-type granites in the region (825–815 Ma; [51]). Therefore, we propose that the Shimensi granodiorite was formed in a collisional/early post collisional setting, as also supported by various tectonic discrimination diagrams (Figure 14). The $\delta^{18}\text{O}$ increase from the Shimensi granodiorite (5.8–7.7‰)

to the younger (819–807 Ma) granodiorite (6.0–8.5‰) in the Jiuling batholith shows an increase of supracrustal rock-derived melts with the progress of collision (Figure 9).

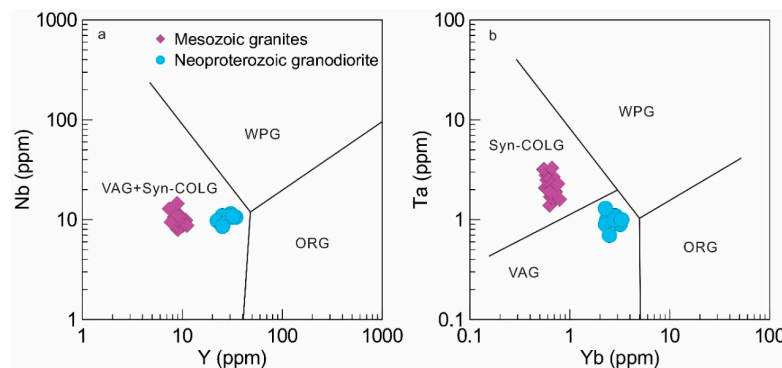


Figure 14. (a) Nb vs. Y; (b) Ta vs. Yb tectonic discrimination diagrams (after Pearce et al. [52]) for the Shimensi granodiorite. VAG, volcanic arc granite; ORG, ocean ridge granite; WPG, within plate granite; syn-COLG and post-COLG, syn- and post-collision granite; COLG, collision granite. Data of the ore-related Mesozoic Shimensi granites are from Wei et al. [6].

At Shimensi, the Neoproterozoic granitoids contain comparable $\text{Ce}^{4+}/\text{Ce}^{3+}$ and Eu/Eu^* values with their Mesozoic counterparts, which are much lower than those of typical porphyry Cu ore-forming intrusions in South China (Figure 15). This shows that the Neoproterozoic Shimensi granodioritic magma is probably too reduced to generate any significant porphyry Cu mineralization. This is consistent with the fact that no ca. 830 to 827 Ma Cu deposits were discovered in the region. In fact, all the Neoproterozoic Cu–Au deposits discovered in the eastern Jiangnan Orogen are much older (1.01–0.98 Ga), and are VMS-type hosted in mafic volcanic rocks [20]. We propose that the lack of porphyry Cu mineralization may have left a high background Cu content (avg. 196 ppm, cf. 80 ppm for the Mesozoic unaltered/unmineralized Shimensi granites) in the Neoproterozoic Shimensi granodiorite, which contributed to the Mesozoic Shimensi W–Cu mineralization while the granodiorite was intruded and assimilated. The assimilation is clearly evidenced by the occurrence of Proterozoic inherited zircons (827 Ma, 829 Ma and 833 Ma) in the Mesozoic Shimensi granites [6], which are closely coeval with the Neoproterozoic granodiorite. Nevertheless, whether (and how much) the Cu in the granodiorite contributed to the Mesozoic W–Cu mineralization at Shimensi will require further investigation.

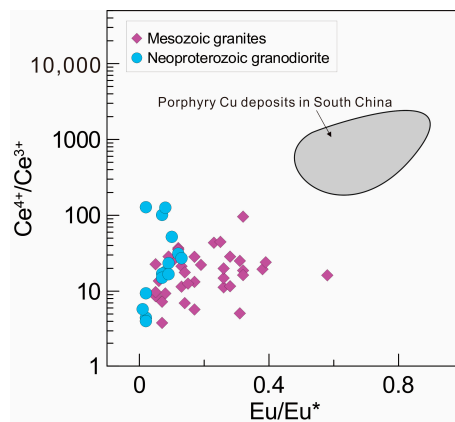


Figure 15. Zircon $\text{Ce}^{4+}/\text{Ce}^{3+}$ vs. Eu/Eu^* for the Shimensi granodiorite. Data of the ore-related Mesozoic Shimensi granites are from Wei et al. [6]. Data source of major porphyry Cu deposits in South China: Dexing [53], Shaxi [54], Dabaoshan [55].

6. Conclusions

In this study, it is found that granodioritic magmatism in the Shimensi area may have commenced around or slightly earlier than many other places in the Jiuling batholith. Whether this represents two separated magmatic phases or one long continuous magmatism is still unknown. The Shimensi granodiorite is best classified as peraluminous I-type formed in a collisional/early post-collisional setting. The lower zircon $\delta^{18}\text{O}$ in the Shimensi granodiorite than many younger granodiorites in the Jiuling batholith shows an increase of supracrustal rock-derived melts with the collision progressed. The low $\text{Ce}^{4+}/\text{Ce}^{3+}$ and Eu/Eu^* values of the Shimensi granodiorite suggested a relatively reduced formation environment, which did not favor porphyry-related Cu–Au mineralization and left a high background Cu concentration in the granodiorite. Whether this high Cu background had contributed to the Mesozoic W–Cu mineralization when the granodiorite was intruded and partially assimilated will require further investigation.

Author Contributions: W.W. contributed significantly to the data analyses and wrote the manuscript. C.L. wrote the manuscript. B.Y. helped perform the analysis with constructive discussions. X.Z. and L.L. drew the figures. S.S. helped perform the literature search.

Funding: National Basic Research Program of China (973 Program, 2014CB440902), National key research and development program (2017YFC0601505) and National Natural Science Foundation of China (No. 41203034; No. 41303030; No. 41673054).

Acknowledgments: This research was financially supported by the National Basic Research Program of China (973 Program, 2014CB440902), National key research and development program (2017YFC0601505) and the National Natural Science Foundation of China (No. 41203034; No. 41303030; No. 41673054). Field work was supported by the Jiangxi No. 916 Geological Team.

Conflicts of Interest: The authors declare no conflicts of interest.

References

1. Mao, J.W.; Xiong, B.K.; Liu, J.; Pirajno, F.; Cheng, Y.B.; Ye, H.S.; Song, S.W.; Dai, P. Molybdenite Re/Os dating, zircon U–Pb age and geochemistry of granitoids in the Yangchuling porphyry W–Mo deposit (Jiangnan tungsten ore belt), China: Implications for petrogenesis, mineralization and geodynamic setting. *Lithos* **2017**, *286–287*, 35–52. [[CrossRef](#)]
2. Dai, P.; Mao, J.W.; Wu, S.H.; Xie, G.Q.; Luo, X.H. Multiple dating and tectonic setting of the Early Cretaceous Xianglushan W deposit, Jiangxi Province, South China. *Ore Geol. Rev.* **2018**, *95*, 1161–1178. [[CrossRef](#)]
3. Zhang, Y.; Gao, J.F.; Ma, D.S.; Pan, J.Y. The role of hydrothermal alteration in tungsten mineralization at the Dahutang tungsten deposit, South China. *Ore Geol. Rev.* **2018**, *95*, 1008–1027. [[CrossRef](#)]
4. Song, W.L.; Yao, J.M.; Chen, H.Y.; Sun, W.D.; Lai, C.K.; Xiang, X.K.; Luo, X.H.; Jourdan, F. A 20 my long-lived successive mineralization in the giant Dahutang W–Cu–Mo deposit, South China. *Ore Geol. Rev.* **2018**, *95*, 401–407. [[CrossRef](#)]
5. Song, W.L.; Yao, J.M.; Chen, H.Y.; Sun, W.D.; Ding, J.Y.; Xiang, X.K.; Zuo, Q.S.; Lai, C.K. Mineral paragenesis, fluid inclusions, H–O isotopes and ore-forming processes of the giant Dahutang W–Cu–Mo deposit, South China. *Ore Geol. Rev.* **2018**, *99*, 115–150. [[CrossRef](#)]
6. Wei, W.F.; Shen, N.P.; Yan, B.; Lai, C.K.; Yang, J.H.; Gao, W.; Liang, F. Petrogenesis of ore-forming granites with implications for W-mineralization in the super-large Shimensi tungsten-dominated polymetallic deposit in northern Jiangxi Province, South China. *Ore Geol. Rev.* **2018**, *95*, 1123–1139. [[CrossRef](#)]
7. Pan, X.F.; Hou, Z.Q.; Zhao, M.; Chen, G.H.; Rao, J.F.; Li, Y.; Wei, J.; Ouyang, Y.P. Geochronology and geochemistry of the granites from the Zhuxi W–Cu ore deposit in South China: Implication for petrogenesis, geodynamical setting and mineralization. *Lithos* **2018**, *304–307*, 155–179. [[CrossRef](#)]
8. Xiang, X.K.; Wang, P.; Sun, D.M.; Zhong, B. Isotopic geochemical characteristics of the Shimensi tungsten-polymetallic deposit in northern Jiangxi province. *Acta Geosci. Sin.* **2013**, *34*, 263–271. (In Chinese)
9. Yuan, S.D.; Williams-Jones, A.E.; Mao, J.W.; Zhao, P.L.; Chen, Y.; Zhang, D.L. The origin of the Zhangjialong tungsten deposit, South China: Implications for W–Sn mineralization in large granite batholiths. *Ecol. Geol.* **2018**, *113*, 1193–1208. [[CrossRef](#)]

10. Mao, Z.H.; Liu, J.J.; Mao, J.W.; Deng, J.; Zhang, F.; Meng, X.Y.; Xiong, B.K.; Xiang, X.K.; Luo, X.H. Geochronology and geochemistry of granitoids related to the giant Dahutang tungsten deposit, middle Yangtze River region, China: Implications for petrogenesis, geodynamic setting, and mineralization. *Gondwana Res.* **2015**, *28*, 816–836. [[CrossRef](#)]
11. Wei, W.F.; Yan, B.; Shen, N.P.; Liu, L.; Zhang, Y.; Xiang, X.K. Muscovite $^{40}\text{Ar}/^{39}\text{Ar}$ Age and H-O-S Isotopes of the Shimensi Tungsten Deposit (Northern Jiangxi Province, South China) and Their Metallogenic Implications. *Minerals* **2017**, *7*, 162. [[CrossRef](#)]
12. Hu, R.Z.; Zhou, M.F. Multiple Mesozoic mineralization events in South China—An introduction to the thematic issue. *Miner. Depos.* **2012**, *47*, 579–588. [[CrossRef](#)]
13. Hu, R.Z.; Bi, X.W.; Jiang, G.H.; Chen, H.W.; Peng, J.T.; Qi, Y.Q.; Wu, L.Y.; Wei, W.F. Mantle-derived noble gases in ore-forming fluids of the granite-related Yaogangxian tungsten deposit, Southeastern China. *Miner. Depos.* **2012**, *47*, 623–632. [[CrossRef](#)]
14. Hu, R.Z.; Fu, S.L.; Huang, Y.; Zhou, M.F.; Fu, S.H.; Zhao, C.H.; Wang, Y.J.; Bi, X.W.; Xiao, J.F. The giant South China Mesozoic low-temperature metallogenic domain: Reviews and a new geodynamic model. *J. Asian Earth Sci.* **2017**, *137*, 9–34. [[CrossRef](#)]
15. Zhou, M.F.; Gao, J.F.; Zhao, Z.; Zhao, W.W. Introduction to the special issue of Mesozoic W-Sn deposits in South China. *Ore Geol. Rev.* **2018**, *10*, 432–436. [[CrossRef](#)]
16. Xie, G.Q.; Mao, J.W.; Bagas, L.; Fu, B.; Zhang, Z.Y. Mineralogy and titanite geochronology of the Caojiaba W deposit, Xiangzhong metallogenic province, southern China: implications for a distal reduced skarn W formation. *Miner. Depos.* **2018**, 1–14. [[CrossRef](#)]
17. Xie, G.Q.; Mao, J.W.; Li, W.; Fu, B.; Zhang, Z.Y. Granite-related Yangjiashan tungsten deposit, southern China. *Miner. Depos.* **2018**, 1–14. [[CrossRef](#)]
18. Hu, R.Z.; Chen, W.T.; Xu, D.R.; Zhou, M.F. Reviews and new metallogenic models of mineral deposits in South China: An introduction. *J. Asian Earth Sci.* **2017**, *137*, 1–8. [[CrossRef](#)]
19. Chen, B.; Gu, H.O.; Chen, Y.J.; Sun, K.K.; Chen, W. Lithium isotope behaviour during partial melting of metapelites from the Jiangnan Orogen, South China: Implications for the origin of REE tetrad effect of F-rich granite and associated rare-metal mineralization. *Chem. Geol.* **2018**, *483*, 372–384. [[CrossRef](#)]
20. Gong, X.D.; Yan, G.S.; Ye, T.Z.; Zhu, X.Y.; Li, Y.S.; Zhang, Z.H.; Jia, W.B.; Yao, X.F. A study of ore-forming fluids in the Shimensi tungsten deposit, Dahutang tungsten polymetallic ore field, Jiangxi Province, China. *Acta Geol. Sin. (Engl. Ed.)* **2015**, *89*, 822–835. [[CrossRef](#)]
21. Zhang, Q.; Zhang, R.Q.; Gao, J.F.; Lu, J.J.; Wu, J.W. In-situ LA-ICP-MS trace element analyses of scheelite and wolframite: Constraints on the genesis of veinlet-disseminated and vein-type tungsten deposits, South China. *Ore Geol. Rev.* **2018**, *99*, 166–179. [[CrossRef](#)]
22. Zuo, Q.S. Analysis on the geological conditions and the assessment of the further ore-finding foreground from Dahutang to Liyangdou metallogenic region in the western part of Jiulingshan, Jiangxi Province. *Resour. Environ. Eng.* **2006**, *20*, 348–353. (In Chinese)
23. Hans Wedepohl, K. The composition of the continental crust. *Geochim. Cosmochim. Acta* **1995**, *59*, 1217–1232. [[CrossRef](#)]
24. Zhao, J.H.; Zhou, M.F.; Zheng, J.P. Constraints from zircon U-Pb ages, O and Hf isotopic compositions on the origin of Neoproterozoic peraluminous granitoids from the Jiangnan Fold Belt, South China. *Contrib. Mineral. Petrol.* **2013**, *166*, 1505–1519. [[CrossRef](#)]
25. Li, X.H.; Li, Z.X.; Ge, W.; Zhou, H.; Li, W.; Liu, Y.; Wingate, M.T.D. Neoproterozoic granitoids in South China: Crustal melting above a mantle plume at ca. 825 Ma? *Precambrian Res.* **2003**, *12*, 45–83. [[CrossRef](#)]
26. Sun, K.K.; Chen, B. Trace elements and Sr-Nd isotopes of scheelite: Implications for the W-Cu-Mo polymetallic mineralization of the Shimensi deposit, South China. *Am. Mineral.* **2017**, *102*, 1114–1128. [[CrossRef](#)]
27. Liang, Q.; Grégoire, D.C. Determination of trace elements in twenty six Chinese geochemistry reference materials by inductively coupled plasma-mass spectrometry. *Geostand. Newsl. J. Geostand. Geoanal.* **2000**, *24*, 51–63. [[CrossRef](#)]
28. Black, L.P.; Kamo, S.L.; Allen, C.M.; Aleinikoff, J.N.; Davis, D.W.; Korsch, R.J.; Foudoulis, C. TEMORA 1: A new zircon standard for Phanerozoic U-Pb geochronology. *Chem. Geol.* **2003**, *200*, 155–170. [[CrossRef](#)]

29. Claoué-Long, J.C.; Compston, W.; Roberts, J.; Fanning, C.M. Two Carboniferous ages: A comparison of SHRIMP zircon dating with conventional zircon ages and $^{40}\text{Ar}/^{39}\text{Ar}$ analyses. In *Geochronology, Time Scales and Global Stratigraphic Correlation*; Special Publication, 54; Berggren, W.A., Kent, D.V., Aubry, M.-P., Hardenbol, J., Eds.; SEPM (Society for Sedimentary Geology): Broken Arrow, OK, USA, 1995; pp. 3–21.
30. Williams, I.S. U-Th-Pb geochronology by ion microprobe. *Rev. Econ. Geol.* **1998**, *7*, 1–35.
31. Cumming, G.L.; Richards, J.R. Ore lead isotope ratios in a continuously changing earth. *Earth Planet. Sci. Lett.* **1975**, *28*, 155–171. [[CrossRef](#)]
32. Ludwig, K.R. *Users Manual for Isoplot/Ex (rev. 2.49): A Geochronological Toolkit for Microsoft Excel*; Berkeley Geochronology Center Special Publication: Berkeley, CA, USA, 2001; pp. 1–55.
33. Ickert, R.B.; Hiess, J.; Williams, I.S.; Holden, P.; Ireland, T.R.; Lanc, P.; Schram, N.; Foster, J.J.; Clement, S.W. Determining high precision, in situ, oxygen isotope ratios with a SHRIMP II: Analyses of MPI-DING silicate-glass reference materials and zircon from contrasting granites. *Chem. Geol.* **2008**, *257*, 114–128. [[CrossRef](#)]
34. Chu, N.C.; Taylor, R.N.; Chavagnac, V.; Nesbitt, R.W.; Boella, R.M.; Milton, J.A.; German, C.R.; Bayon, G.; Burton, K. Hf isotope ratio analysis using multi-collector inductively coupled plasma mass spectrometry: An evaluation of isobaric interference corrections. *J. Anal. At. Spectrom.* **2002**, *17*, 1567–1574. [[CrossRef](#)]
35. Woodhead, J.; Hergt, J.; Shelley, M.; Eggins, S.; Kemp, R. Zircon Hf-isotope analysis with an excimer laser, depth profiling, ablation of complex geometries, and concomitant age estimation. *Chem. Geol.* **2004**, *209*, 121–135. [[CrossRef](#)]
36. Bouvier, A.; Vervoort, J.D.; Patchett, P.J. The Lu-Hf and Sm-Nd isotopic composition of CHUR: Constraints from unequilibrated chondrites and implications for the bulk composition of terrestrial planets. *Earth Planet. Sci. Lett.* **2008**, *273*, 48–57. [[CrossRef](#)]
37. Griffin, W.L.; Wang, X.; Jackson, S.E.; Pearson, N.J.; O'Reilly, S.Y.; Xu, X.; Zhou, X. Zircon chemistry and magma mixing, SE China: In-situ analysis of Hf isotopes, Tonglu and Pingtan igneous complexes. *Lithos* **2002**, *61*, 237–269. [[CrossRef](#)]
38. Liu, Y.S.; Hu, Z.C.; Gao, S.; Günther, D.; Xu, J.; Gao, C.G.; Chen, H.H. In situ analysis of major and trace elements of anhydrous minerals by LA-ICP-MS without applying an internal standard. *Chem. Geol.* **2008**, *257*, 34–43. [[CrossRef](#)]
39. Griffin, W.L.; Powell, W.J.; Pearson, N.J.; O'Reilly, S.Y. GLITTER: Data reduction software for laser ablation ICP-MS. In *Laser Ablation-ICP-MS in the Earth Sciences*; Mineralogical Association of Canada Short Course Series; Sylvester, P., Ed.; Mineralogical Association of Canada: Quebec City, QC, Canada, 2008; Volume 40, pp. 204–207.
40. Hoskin, P.W.O.; Schaltegger, U. The composition of zircon and igneous and metamorphic petrogenesis. *Rev. Mineral. Geochem.* **2003**, *53*, 27–62. [[CrossRef](#)]
41. Sun, S.S.; McDonough, W.F. Chemical and isotopic systematics of ocean basalts: Implications for mantle composition and processes. *Geol. Soc. Lond. Spec. Publ.* **1989**, *42*, 313–346. [[CrossRef](#)]
42. Hoskin, P.; Black, L.P. Metamorphic zircon formation by solid-state recrystallization of protolith igneous zircon. *J. Metamorph. Geol.* **2000**, *18*, 423–439. [[CrossRef](#)]
43. Wang, X.L.; Zhou, J.C.; Wan, Y.S.; Kitajima, K.; Wang, D.; Bonamici, C.; Qiu, J.S.; Sun, T. Magmatic evolution and crustal recycling for Neoproterozoic strongly peraluminous granitoids from southern China: Hf and O isotopes in zircon. *Earth Planet. Sci. Lett.* **2013**, *366*, 71–82. [[CrossRef](#)]
44. Whitehouse, M.J.; Platt, J.P. Dating high-grade metamorphism—Constraints from rare-earth elements in zircon and garnet. *Contrib. Mineral. Petrol.* **2003**, *145*, 61–74. [[CrossRef](#)]
45. Dilles, J.H.; Kent, A.J.R.; Wooden, J.L.; Tosdal, R.M.; Koleszar, A.; Lee, R.G.; Farmer, L.P. Zircon compositional evidence for sulfur-degassing from ore-forming arc magmas. *Econ. Geol.* **2015**, *110*, 241–251. [[CrossRef](#)]
46. Ballard, J.R.; Palin, M.J.; Campbell, I.H. Relative oxidation states of magmas inferred from Ce(IV)/Ce(III) in zircon: Application to porphyry copper deposits of northern Chile. *Contrib. Mineral. Petrol.* **2002**, *144*, 347–364. [[CrossRef](#)]
47. Trail, D.; Bruce Watson, E.; Tailby, N.D. Ce and Eu anomalies in zircon as proxies for the oxidation state of magmas. *Geochim. Cosmochim. Acta* **2012**, *97*, 70–87. [[CrossRef](#)]
48. Chappell, B.W.; White, A.J.R. Two contrasting granite types: 25 years later. *Aust. J. Earth Sci.* **2001**, *48*, 489–499. [[CrossRef](#)]

49. Belousova, E.; Griffin, W.; O'Reilly, S.Y.; Fisher, N. Igneous zircon: Trace element composition as an indicator of source rock type. *Contrib. Mineral. Petrol.* **2002**, *143*, 602–622. [[CrossRef](#)]
50. Zhao, G.C. Jiangnan Orogen in South China: Developing from divergent double subduction. *Gondwana Res.* **2015**, *27*, 1173–1180. [[CrossRef](#)]
51. Wang, G.G.; Ni, P.; Zhu, A.D.; Wang, X.L.; Li, L.; Hu, J.S.; Liu, W.H.; Huang, B. 1.01–0.98Ga mafic intra-plate magmatism and related Cu-Au mineralization in the eastern Jiangnan orogen: Evidence from Liuji and Tieshajie basalts. *Precambrian Res.* **2018**, *309*, 6–21. [[CrossRef](#)]
52. Pearce, J.A.; Harris, N.B.W.; Tindle, A.G. Trace element discrimination diagrams for the tectonic interpretation of granitic rocks. *J. Petrol.* **1984**, *25*, 956–983. [[CrossRef](#)]
53. Zhang, H.; Ling, M.X.; Liu, Y.L.; Tu, X.L.; Wang, F.Y.; Li, C.Y.; Liang, H.Y.; Yang, X.Y.; Arndt, N.T.; Sun, W.D. High oxygen fugacity and slab melting linked to Cu mineralization: Evidence from Dexing porphyry copper deposits, Southeastern China. *J. Geol.* **2013**, *121*, 289–305. [[CrossRef](#)]
54. Deng, J.H.; Yang, X.Y.; Li, S.; Gu, H.L.; Mastoi, A.S.; Sun, W.D. Partial melting of subducted paleo-Pacific plate during the early Cretaceous: Constraint from adakitic rocks in the Shaxi porphyry Cu–Au deposit, Lower Yangtze River Belt. *Lithos* **2016**, *262*, 651–667. [[CrossRef](#)]
55. Li, N.; Chen, Y.J.; Pirajno, F.; Gong, H.J.; Mao, S.-D.; Ni, Z.Y. LA-ICP-MS zircon U–Pb dating, trace element and Hf isotope geochemistry of the Heyu granite batholith, eastern Qinling, central China: Implications for Mesozoic tectono-magmatic evolution. *Lithos* **2012**, *142–143*, 34–47. [[CrossRef](#)]



© 2018 by the authors. Licensee MDPI, Basel, Switzerland. This article is an open access article distributed under the terms and conditions of the Creative Commons Attribution (CC BY) license (<http://creativecommons.org/licenses/by/4.0/>).